Scalar Magnetometry Below 100 fT/Hz$^{1/2}$ in a Microfabricated Cell

Vladislav Gerginov, Marco Pomponio, and Svenja Knappe

***Abstract*—Zero-field optically-pumped magnetometers are a room-temperature alternative to traditionally used superconducting sensors detecting extremely weak magnetic fields. They offer certain advantages such as small size, flexible arrangement, reduced sensitivity in ambient fields offering the possibility for telemetry. Devices based on microfabricated technology are nowadays commercially available. The limited dynamic range and vector nature of the zero-field magnetometers restricts their use to environments heavily shielded against magnetic noise. Total-field (or scalar) magnetometers based on microfabricated cells have demonstrated subpicotesla sensitivities only recently. This work demonstrates a scalar magnetometer based on a single optical axis, 18 $(3 \times 3 \times 2)$ mm^3 microfabricated cell, with a noise floor of 70 fT/Hz$^{1/2}$. The magnetometer operates in a large static magnetic field range, and and is based on a simple optical and electronic configuration that allows the development of dense sensor arrays. Different methods of magnetometer interrogation are demonstrated. The features of this magnetic field sensor hold promise for applications of miniature sensors in nonzero field environments such as unshielded magnetoencephalography (MEG) and brain-computer interfaces (BCI).**

***Index Terms*—Magnetometry, MEMS, Optically-Pumped Magnetometer, Total-Field Magnetometer**

I. Introduction

THE zero-field atomic magnetometers based on microfabricated vapor cells have demonstrated their use in various applications such as biomagnetism [1], low-field NMR [2]–[4], particle detection [5] and microwave field strength measurements [6]. Based on optical pumping in alkali atoms and exploiting the spin-exchange relaxation-free (SERF) regime [7], [8], they offer sensitivities rivaling those of Superconducting Quantum Interference Devices (SQUIDs) [9] and advantages such as room temperature operation, reduced size, and the possible implementation of flexible, wearable sensor arrays for imaging. Despite their success, the small dynamic range and the vector nature of the zero-field sensors currently restrict their application to magnetically shielded environments that provide ultra-low, homogeneous and stable residual background field.

The total-field magnetometers have larger dynamic range extending to Earth's magnetic field of $\sim$50 μT, enabling applications in finite and varying fields. These magnetometers are only sensitive to changes in the total field magnitude, and largely immune to noise in directions orthogonal with respect to the one of the total field. They are also less sensitive to small misalignment and rotation with respect to the magnetic field direction. This allows for higher common suppression important in gradiometry. For this reason, they have traditionally been chosen for magnetic measurements from moving platforms, for example, for geophysics, unexploded ordnance detection, and magnetic anomaly detection. In addition, as they can measure the precession of the atomic polarization (Larmor precession), which is proportional to the strength of the bias magnetic field and the atomic gyromagnetic ratio. In certain implementations they can provide calibration-free magnetic field measurement related to fundamental constants [10], [11]. In contrast, the zero-field magnetometers are based on absorption or polarization rotation measurements and need calibration.

Total-field magnetometers are usually limited by spin-exchange collision resonance broadening, and their sensitivity is typically less than in SERF based zero-field ones. The total-field magnetometers have broader magnetic resonances, operate at lower atomic vapor densities, and suffer from inefficient optical pumping due to the detrimental effect of the nonzero magnetic field. Nevertheless, a total-field magnetomemeter noise floor below 1 fT/Hz$^{1/2}$ has been demonstrated with a 660 mm^3 sensitive volume multipass vapor cell [12]. Recently, magnetoencephalography (MEG) measurements requiring fT-level sensitivities have been performed in an unshielded Earth's field environment [13], reaching magnetometer noise floor of 50 fT/Hz$^{1/2}$ and a gradiometer sensitivity of 16 fT/cm/Hz$^{1/2}$ in a 800 mm^3 sensitive volume.

For many applications, there is a need for device miniaturization. For example, brain activity imaging for MEG or brain-computer interfaces (BCI) requires dense arrays of non-overlapping sensors to achieve high resolution. SQUID-based brain imaging instruments for MEG feature more than 300 sensors close to a person's head, and similar sensor density is needed for imaging with optically-pumped magnetometers. The first total-field magnetometer featuring microfabricated vapor cell had a sensitivity of 50 pT/Hz$^{1/2}$. Significant progress has been made since, with several groups reporting noise floors at the pT/Hz$^{1/2}$ level and below [14]–[16]. Microfabricated OPMs have allowed for millimeter-size active volume and a noise floor below 150 fT/Hz$^{1/2}$ in a gradiometer mode [17], predicting the possibility to achieve magnetometer noise floor below 100 fT/Hz$^{1/2}$ [14], [17].

This work presents a single optical axis ^{87}Rb magnetometer based on single-pass microfabricated vapor cell with 18 $(3 \times 3 \times 2)$ mm^3 sensitive volume. The magnetometer has a noise floor of 70 fT/Hz$^{1/2}$, and can be interrogated in a synchronous or pulsed optical excitation scheme, facilitating measurements in varying magnetic fields with reduced sensor complexity. The noise floor is similar to the one of the first

V. Gerginov, M. Pomponio and S. Knappe are with theDepartment of Mechanical Engineering, University of Colorado Boulder, Boulder, CO, USA

reported microfabricated single-axis zero-field SERF magnetometer [18]. The magnetometer's optical pumping process in pulsed operation is modified, allowing highly efficient optical pumping in the full, but not limited to, 1 to 11 μT range of measured ambient magnetic fields. Due to the single axis operation, the sensor exhibits a polar deadzone, preferable to the equatorial deadzone of most magnetometers with perpendicular pump and probe beams. This allows to use two instead of three magnetometers for deadzone-free operation.

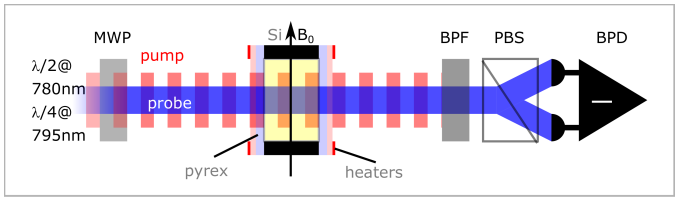

Fig. 1. Physics package setup. MWP - multi-order wave plate. BPF - bandpass filter. PBS - polarizing beamsplitter (Wollaston prism). BPD - balanced photodetector.

II. Experimental Section

The experimental setup is shown in Figure 1. The magnetometer uses a pump and a probe laser beam. The unmodulated probe light at 780.152(1) nm is blue-detuned by $\sim$ 50 GHz from the pressure-shifted and broadened ^{87}Rb D_2 line [19] in a microfabricated vapor cell, which is filled with ^{87}Rb and 800 Torr nitrogen as a buffer gas. The AM modulated pump light at 794.992(1) nm is on resonance with the pressure-broadened and shifted ^{87}Rb D_1 line [19]. Both beams are collimated to $\sim$ 3 mm diameters (full-width at half-maximum), overlapped, and co-propagate through a multiple-order waveplate (as demonstrated in previous work [20], [21]) before entering the $3 \times 3\,\text{mm}^2$ vapor cell entrance window. The laser wavelengths were not stabilized during the experiment and were within $\pm$1 GHz from the wavelengths specified above over the course of the measurements. The waveplate converts the pump beam's linear polarization into a circular one, and rotates the probe beam's linear polarization while keeping it linear. The beams propagate through the vapor cell with $3\times3\times2\,\text{mm}^3$ inner-dimensions, which is heated to a temperature of $\sim$373 K. The cell heating is done with nonmagnetic AC current-driven heaters attached on the cell windows, providing optical access to the cell. The vapor cell is placed in a highly homogeneous and stable bias field B_0. After the cell, the pump light is blocked by a 1 nm full-width at half-maximum bandpass filter. The polarization state of the probe light is analyzed with a polarimeter based on a Wollaston prism, and detected with a 100 kHz-bandwidth balanced photodetector.

The amplitude modulation of the pump laser light is performed with an acousto-optic modulator (AOM), driven by a train of RF pulses with a variable duty cycle. The pump laser system delivers $\sim$170 mW fiber-coupled peak power, approximately 50% of which is sent to the vapor cell. The probe laser beam has $\sim$4 mW in front of the vapor cell, and the $\sim$2 mW output power is distributed between the two arms of the polarimeter shown in Figure 1. The lasers are manually tuned to the wavelengths optimizing the magnetometer signal, and are free-running during the measurements.

A digital lock-in amplifier reference is synchronized to the RF pulse train driving the AM modulation of the pump laser for the Bell-Bloom scheme of magnetometer operation (see Section III-A). The lock-in amplifier is a commercial device with 60 MHz, 16-bit input channel and 500 kHz bandwidth. For the magnetic field tracking scheme (see Section III-E), the lock-in amplifier is internally referenced and provides a TTL logic trigger for the pump laser pulse train.

An FPGA board [22] and its Software Development Kit (SDK) [23] are used for the Free Induction Decay (FID) scheme of magnetometer operation (see Section III-B). This board implements two 14-bit ADCs running at 250 MSps. On the processor side a Linux operating system allows to receive commands through TCP/IP protocol from python scripts. An input decimator stage trades the high sampling rate of the fast ADC for more resolution [24], gaining 1 bit every decimation by 4. It is implemented using a configurable cascaded integrator-comb (CIC) filter and a finite impulse response (FIR) correction filter, and has 6 available total decimation rates from 64 to 2048 in powers of 2 (bit gains from 3 to 5.5). For the present experiment, we use a decimation rate of 64. The stream of data is sent to the board's RAM memory through DMA (Direct Memory Access) in which a total of 64 MB, or 8 M samples for each channel, is allocated. When the sampling is complete the data can be accessed using a python script.

III. Results

The experimental details on the hardware implementation can be found in Section II. The optically-driven magnetometer can be operated in a synchronous or pulsed schemes. Below is the comparison between the two schemes that use detection of spin precession [25] in a bias magnetic field. Synchronously-driven optical excitation, or Bell-Bloom, scheme [17], [26]–[31] is used as a benchmark for comparison against pulsed optical excitation, or Free Induction Decay [11], [15], [32]–[34].

A. Bell-Bloom (synchronous) pumping scheme

The synchronously-driven optical spin excitation is implemented by amplitude modulation (AM) of the pump laser beam. The frequency of the AM modulation (or its harmonic) is used to reference a digital lock-in amplifier to perform a phase detection of the Larmor precession. Figure 2, top plot shows a typical polarimeter signals at two reference frequencies as a function of the bias magnetic field. Figure 2, bottom plot shows the quadrature signals after demodulation as a function of the bias magnetic field. The magnetic noise floor of the sensor is measured at a bias magnetic field corresponding to the steepest slope of the demodulated signals in the vicinity of the signal zero crossing, as indicated with the ellipse. The conversion factor between measured voltage and magnetic field is determined by the lock-in amplifier voltage

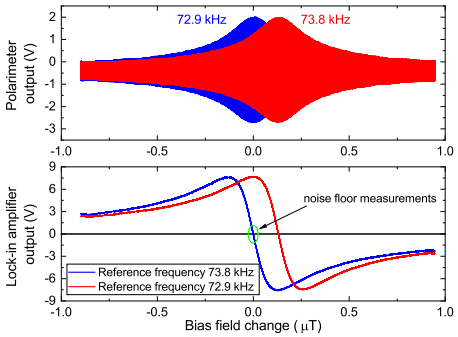

Fig. 2. Polarimeter output signal (top plot) and quadrature lock-in signal (bottom plot) as a function of the bias magnetic field around $B_0 = 10.54\,\mu$T. The pump light AM frequency was set to 72.9 kHz and 73.8 kHz, respectively. The lock-in amplifier reference frequency was locked to the AM frequency.

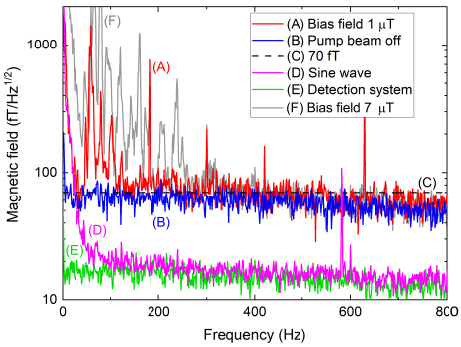

Fig. 3. Magnetic field noise spectrum. Trace (A) - $B_0 = 1\,\mu$T. Trace (B) - pump beam off. Trace (C) - 70 fT level. Trace (D) - equivalent noise of a sine wave input. Trace (E) - equivalent noise with the probe beam off. Trace (F) - $B_0 = 7\,\mu$T.

change corresponding to a change in the AM modulation frequency.

The pump-pulse duration determined by the AM duty cycle is much shorter than the Larmor precession period. Due to the limited pumping peak power and the lower limit of the pump-pulse length to above 1 μs determined by the AOM, the highest degree of atomic polarization and the best magnetometer sensitivity are reached at low bias fields on the order of $\sim 1\,\mu$T.

Figure 3 trace (A) shows the measured magnetic field noise at 1 μT bias field. The measured magnetic field noise is at a 70 fT/Hz$^{1/2}$ level away from noise spikes. Trace (B) shows the measured detection noise in the absence of optical pumping, which is at or below the 70 fT/Hz$^{1/2}$ level, as indicated by the dashed line (trace (C)). It is also consistent with the level of photon shot noise due to the $\sim$0.5 mW probe light per polarimeter channel. Trace (D) shows the equivalent noise when a sinusoidal signal from a function generator is sent to the input of the lock-in amplifier. It shows increased noise floor at low frequencies (below 20 Hz), either due to the phase noise of the function generator or the PLL noise of the lock-in amplifier reference input. Trace (E) shows the effective noise contribution from the detection system that is below 20 fT/Hz$^{1/2}$ in the absence of light signal on the polarimeter. Trace (F) shows magnetic field noise spectrum at bias field B_0=7μT. It can be seen that the low-frequency increases at higher bias fields, limited by the noise of current source producing the field itself.

Figure 3 shows a slight signal roll-off at higher frequencies, which is due to the combination of the magnetometer's bandwidth of $\sim$1 kHz and the lock-in amplifier time constant of 0.1 ms.

B. FID (pulsed) interrogation scheme

1) Optical pumping in finite bias field: The pulsed operation of the magnetometer (FID scheme) is implemented by AM modulation of the pump light at a repetition rate of 1 kHz. The pumping phase is followed by a spin precession detection phase. The pumping pulse results in spin precession that causes a decaying oscillating signal at the polarimeter output. The spin precession at a Larmor frequency of 100 kHz (bias field of 14.3 μT orthogonal to the laser beam direction) is shown in Figure 4. Trace (A) shows a typical FID signal measurement cycle with the value of the bias magnetic field is the same during the pump and probe phases. The pump phase lasts 5.2 μs, which is found to optimize the FID signal amplitude. The FID signal amplitude decays exponentially with a time constant of $\sim$300 μs, which has a significant contribution by spin-exchange relaxation due to atom-atom collisions. One of the advantages of the FID mode when compared to other methods that use magnetic field modulation is that it is magnetically quiet, which means less cross-talk with neighboring sensors, when placed in dense arrays.

2) Optical pumping in zero bias field: The finite bias field orthogonal to the pump beam orientation has a detrimental effect on the degree of atomic polarization. The reason is that in this case the atomic state prepared by the process of optical pumping is not an eigenstate of the atomic system with quantization axis along the bias field. The magnetic field causes a temporal evolution of the optically pumped atomic state (spin precession), thus counteracting the effect of optical pumping. Methods exist for creating a high degree of atomic polarization. Highly efficient optical pumping in the bias field parallel to the pump beam direction can be performed, followed by a rotation of the atomic polarization by 90° with a π/2 RF pulse [35]. Another method is the addition of a strong magnetic field in the direction of the pump beam during the optical pumping phase, aligning the total field mostly in the direction of the pump field [36]. An additional possibility is the use of short, intense optical pumping pulse train that is synchronous with the atomic precession frequency [37].

A different approach is implemented in this work. The bias magnetic field during the pump phase is zeroed by adding temporarily a magnetic field in the opposite direction to the existing bias field. This allows the optical pumping phase to be extended compared to the 5.2 μs in the case of finite field pumping. With the zeroing pulse, the optical pumping phase duration which optimizes the optical pumping is 80 μs. Figure 4 trace (B) shows the signal resulting from the modified FID signal measurement cycle. The signal amplitude is $\sim$8 times higher (compare traces (B) and (C)), indicating a higher degree of atomic polarization, and more

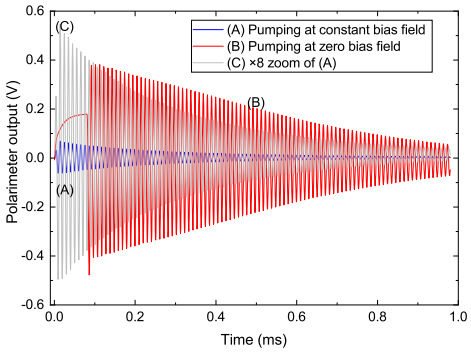

Fig. 4. Polarimeter output signal versus time, FID scheme. Trace (A) - optical pumping in finite bias field with 5.2 μs duration. Trace (B) - optical pumping in zero bias field with 80 μs duration. Trace (C) - $\times 8$ zoom of trace (A).

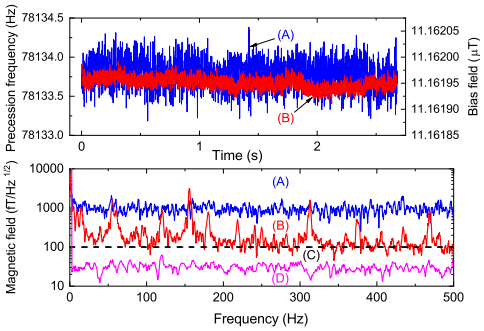

Fig. 5. Top plot - FID frequency and corresponding magnetic field values as a function of time. Trace (A) - field zeroing off. Trace (B) - field zeroing on. Bottom plot - magnetic field noise spectrum calculated from the measured FID frequency. Trace (A) - field zeroing off. Trace (B) - field zeroing on. Trace (C) - 100 fT level. Trace (D) - equivalent noise floor of a sine wave input signal.

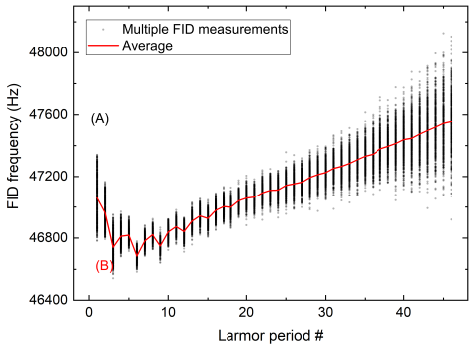

Fig. 6. FID frequency as a function of precession period number. Trace (A) - single-period analysis of multiple FID signals. Trace (B) - average of all FID signals.

efficient transfer of the atomic population to the stretched atomic state $|F = 2, m_F = F\rangle$ of the ^{87}Rb ground state. The following FID signal measurement reveals a non-exponential signal decay due to the suppressed spin-exchange relaxation caused by atom-atom collisions at high degree of atomic polarization [38]. Further indication for this effect is the increased coherence time of the atomic system - an exponential decay analysis reveals a time constant of $\sim$535 μs. The use of zeroing magnetic pulse allows to reduce the required optical pumping power by increasing the duration of optical pumping.

The FID signals, such as the ones shown in Figure 4, are obtained at a repetition rate of 1 kHz and analyzed using a nonlinear fit model of a decaying sinusoidal. The frequency of the sinusoidal as a function of measurement time is shown in Figure 5. Figure 5, top plot, trace (A) represents frequency measurements performed with optical pumping in finite bias fields. The corresponding magnetic field spectrum is shown in Figure 5, bottom plot, trace (A). The frequency measurements with optical pumping in zero field are shown in Figure 5, traces (B). They show a reduced noise floor by an order of magnitude - the result of increased signal amplitude and longer signal decay time constant. The trace shows spectral components with amplitude as high as 1 pT/Hz$^{1/2}$, the origin of which is unknown, but is possibly related to the digital sampling of the FID signal at a frequency that is not phase-synchronized with the repetition rate of the FID signal, combined with FID signal frequency evolution, which is discussed below. At the same time, trace (B) shows the noise spectrum reaching 100 fT (trace C) away from the discrete spectral components. Analysis of a sinusoidal signal sent to the FPGA board from a function generator, shown by Figure 5, bottom plot, trace (D), is indication that measurements with 30 fT/Hz$^{1/2}$ noise floor are possible with this specific hardware. This noise floor is slightly higher than the corresponding measurement shown in Figure 3, trace (D), but in contrast to it, shows no increase at frequencies below 20 Hz, and is not affected by the low-pass filter used for the lock-in amplifier measurements.

C. Nonlinearities in the measured FID signal frequency

The fit residuals show a nonlinear time dependence of the FID signal frequency (frequency chirp), whose origin has not been investigated in detail in this work but is most likely due to the nonlinear dynamics of the spin-exchange relaxation [35].

The FID frequency evolution can be visualized by partitioning each FID signal into non-overlapping precession periods, and analyzing their individual frequencies. Figure 6 shows the FID frequency of each non-overlapping periods as a function of precession period number after the start of the FID detection. Trace (A) shows the analysis of multiple FID measurements. Trace (B) shows the averaged value of the measured frequencies over the all FID measurements. The results shown in Figure 6 show nonlinearities in the FID frequency that persist for several precession periods of $\sim$ 20 μs. These nonlinearities cannot be explained by light shift caused by the presence of pump light during the FID measurements, since the fall-time of the pump-pulse is < 1 μs.

D. Gated lock-in amplifier for FID frequency acquisition

The pulsed FID mode of operation requires the use of a gated lock-in amplifier, as the FID signal is present only during the detection phase of the magnetometer cycle. The use of a gated lock-in amplifier allows to acquire a single FID precession frequency value for each magnetometer cycle. During the detection phase of a given magnetometer cycle, the gated lock-in amplifier performs several measurements of

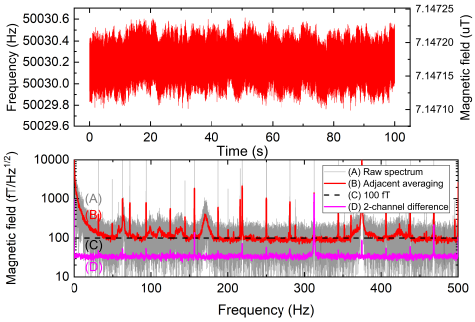

Fig. 7. Top plot - FID frequency and corresponding magnetic field. Bottom plot - magnetic field noise spectrum calculated from the measured FID frequency. Trace (A) - raw spectrum. Trace (B) - smoothed raw data using adjacent averaging. Trace (C) - 100 fT level. Trace (D) - differential measurement using the same input signal on the inputs of two independent lock-in amplifier channels.

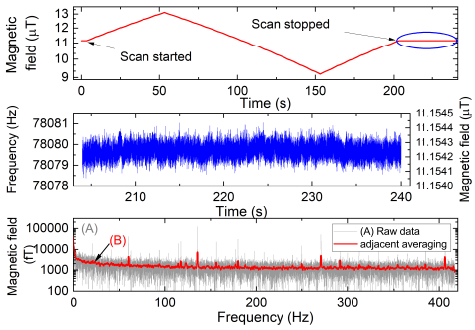

Fig. 8. Magnetic field tracking measurement. Top plot - magnetic field scan as a function of measurement time. Middle plot - Larmor precession frequency and magnetic field magnitude after the field scan was stopped. Bottom plot - magnetic field noise spectrum calculated from the data shown in the middle plot. Trace (A) - raw spectrum. Trace (B) - smoothed raw data using adjacent averaging.

the phase difference between the lock-in reference signal and the FID signal. The phase difference values are converted to frequency difference values using the time reference of the lock-in amplifier, resulting in data similar to the one shown in Fig. 6. A linear regression is used to determine an average frequency difference value, which is added to the lock-in amplifier reference frequency. The resulting frequency represents the FID precession frequency during the given magnetometer cycle. As the magnetometer cycles repeat, the lock-in amplifier streams frequency values at a millisecond rate. A low-pass filter with a cutoff frequency of several kilohertz is implemented to reduce the noise in the resulting frequency data stream. Figure 7 (top) shows such a Larmor precession frequency stream as a function of time. The corresponding calculated magnetic field is shown on the right scale. Figure 7 (bottom , trace (A)) shows the magnetic field noise spectrum. Trace (B) shows the averaged magnetometer noise floor reaching a 100 fT/Hz$^{1/2}$ level (trace (C)). To assess the performance of the gated lock-in, the FID signal is sent to the second, independent channel of the lock-in. Figure 7 (trace (D)) shows the resulting spectrum after the frequency data from each channel has been subtracted, and demonstrates that the gated lock-in amplifier allows measurements with a noise floor below 30 fT/Hz$^{1/2}$.

E. Magnetic field tracking

The use of gated lock-in amplifier, combined with the FID operation of the magnetometer allows to measure varying magnetic fields. Each measurement cycle is independent and provides high-resolution information about the magnitude of the measured magnetic field, extracted from the measured precession frequency. The obtained field magnitude can be compared to the previous value, allowing for adjustment of the reference frequency of the local oscillator for the next measurement cycle. Figure 8 shows a proof-of-principle field tracking measurement performed with the gated lock-in amplifier. Figure 8, top plot, shows the measured magnetic field scanned over 4 μT. The field scan is limited by the dynamic range of the current source modulation input, and not by the magnetometer. Figure 8, middle plot shows the measured magnetic field after the field scan was terminated. The magnetic field spectrum and its average using adjacent averaging are shown in Figure 8, bottom plot, by traces (A) and (B), respectively. The measurement noise floor is limited to above 1 pT/Hz$^{1/2}$ since the optical pumping phase is performed in finite bias fields. If field zeroing is implemented during the pumping phase by setting the zeroing field magnitude to the measured bias field value during the preceding FID cycle, the measurement noise floor is expected to reach 100 fT/Hz$^{1/2}$ as shown in Section III-B2 and in Figure 7.

IV. Discussion

Section III shows that millimeter size microfabricated vapor cells support magnetic field magnitude (scalar) measurements with noise floor below 100 fT/Hz$^{1/2}$. The optical configuration is simple and compatible with the established single-axis anodic bonding cell fabrication technology [39]. The sensor exhibits a polar deadzone, which is preferrable to the equatorial deadzone of magnetometers featuring orthogonal pump and probe light geometries.

Magnetic field values can be obtained using optically-driven spin precession in synchronous or pulsed scheme. The synchronous scheme results in the lowest noise floor of 70 fT/Hz$^{1/2}$, determined by photon shot noise. The synchronous scheme works best at low bias magnetic fields, as the duration of the periodic optical pumping is limited to a fraction of the Larmor precession frequency, limiting the optical pumping efficiency and the achievable degree of atomic polarization at high precession frequencies.

In the pulsed scheme, the optical pumping phase is modified to achieve high degree of atomic polarization, resulting in a higher measurement signal-to-noise, and achieving 100 fT/Hz$^{1/2}$ noise floors at bias fields above 10 μT. This scheme of operation does not necessarily require synchronization of the optical pumping pulses with the atomic precession frequency, or a phase detection. The demonstrated data acquisition schemes show detection noise floors at or below 30 fT/Hz$^{1/2}$. The pulsed interrogation scheme has been demonstrated with a gated lock-in amplifier phase detection, resulting in a similar magnetometer performance.

A magnetic field tracking with measurement noise floor of $1\,\mathrm{pT/Hz^{1/2}}$ is demonstrated by exploiting the large dynamic range of the total-field (scalar) magnetometers. The field tracking measurement is compatible with the modified optical pumping scheme that increases the atomic polarization using bias field zeroing. To fully benefit from the modified optical pumping scheme for magnetic field tracking, the measured magnetic field values could be used to adjust the field zeroing between measurement cycles, realizing a closed loop for the field zeroing coils with a bandwidth determined by the repetition rate of the field measurements, typically around 1 kHz.

The magnetometer noise floor is limited by the photon shot noise of the probe light field. The noise floor could be lowered by implementing a multipass vapor cell configuration, as demonstrated with larger cells [13]. An intrinsic gradiometer configuration [40] can also be used, in which the photon shot noise will be common-mode.

V. Conclusion

The microfabricated vapor cell technology [39] has enabled the commercialization of chip-scale atomic devices [41]. The need for room-temperature wearable sensors for biomagnetism has driven the commercial interest in zero-field atomic magnetometers [42], but these still require extreme magnetic field control. The total-field magnetometers offer the possibility to perform unshielded biomagnetism measurements [13] or perform highly sensitive magnetic field measurements with a large dynamic range, although much research and development is still needed to suppress the spatially and temporally-varying ambient noise. Forming dense imaging arrays based on hundreds of sensors requires small footprint, low cross-talk, simple optical arrangement, and low-cost batch fabrication [17]. The results of this work show progress towards microfabricated total-field magnetic sensors with sub $100\,\mathrm{fT/Hz^{1/2}}$ noise floors, based on single-pass, single optical axis configuration with reduced sensor complexity and footprint.

Acknowledgment

The authors would like to thank Dr. Tobias Thiele (Zurich Instruments) for the help with the gated lock-in amplifier data acquisition. This work was supported by The Defense Advanced Research Projects Agency (N3 program, N6523619C8013) and the National Institute of Health (R01EB027004). The views, opinions, and/or findings contained in this article are those of the author and should not be interpreted as representing the official views or policies, either expressed or implied, of the Defense Advanced Research Projects Agency or the Department of Defense.

References

[1] T. H. Sander, J. Preusser, R. Mhaskar, J. Kitching, L. Trahms, and S. Knappe, "Magnetoencephalography with a chip-scale atomic magnetometer," *Biomedical Optics Express*, vol. 3, no. 5, pp. 981–990, Apr. 2012. [Online]. Available: http://www.ncbi.nlm.nih.gov/pmc/articles/PMC3342203/

[2] M. P. Ledbetter, I. M. Savukov, D. Budker, V. Shah, S. Knappe, J. Kitching, D. J. Michalak, S. Xu, and A. Pines, "Zero-field remote detection of NMR with a microfabricated atomic magnetometer," *Proceedings of the National Academy of Sciences*, vol. 105, no. 7, pp. 2286–2290, 2008. [Online]. Available: http://www.pnas.org/content/105/7/2286

[3] T. Theis, P. Ganssle, G. Kervern, S. Knappe, J. Kitching, M. P. Ledbetter, D. Budker, and A. Pines, "Parahydrogen-enhanced zero-field nuclear magnetic resonance," *Nat Phys*, vol. 7, no. 7, pp. 571–575, Jul. 2011. [Online]. Available: http://dx.doi.org/10.1038/nphys1986

[4] R. Jimenez-Martinez, D. J. Kennedy, M. Rosenbluh, E. A. Donley, S. Knappe, S. J. Seltzer, H. L. Ring, V. S. Bajaj, and J. Kitching, "Optical hyperpolarization and NMR detection of 129Xe on a microfluidic chip," *Nat. Commun.*, vol. 5, pp. –, May 2014. [Online]. Available: http://dx.doi.org/10.1038/ncomms4908

[5] D. Maser, S. Pandey, H. Ring, M. P. Ledbetter, S. Knappe, J. Kitching, and D. Budker, "Note: Detection of a single cobalt microparticle with a microfabricated atomic magnetometer," *Review of Scientific Instruments*, vol. 82, no. 8, p. 086112, 2011. [Online]. Available: https://doi.org/10.1063/1.3626505

[6] A. Horsley, G.-X. Du, M. Pellaton, C. Affolderbach, G. Mileti, and P. Treutlein, "Imaging of relaxation times and microwave field strength in a microfabricated vapor cell," *Phys. Rev. A*, vol. 88, p. 063407, Dec 2013. [Online]. Available: https://link.aps.org/doi/10.1103/PhysRevA.88.063407

[7] W. Happer and H. Tang, "Spin-exchange shift and narrowing of magnetic resonance lines in optically pumped alkali vapors," *Phys. Rev. Lett.*, vol. 31, pp. 273–276, Jul 1973. [Online]. Available: http://link.aps.org/doi/10.1103/PhysRevLett.31.273

[8] J. C. Allred, R. N. Lyman, T. W. Kornack, and M. V. Romalis, "High-sensitivity atomic magnetometer unaffected by spin-exchange relaxation," *Phys. Rev. Lett.*, vol. 89, p. 130801, Sep 2002. [Online]. Available: http://link.aps.org/doi/10.1103/PhysRevLett.89.130801

[9] R. Körber, J.-H. Storm, H. Seton, J. P. Mäkelä, R. Paetau, L. Parkkonen, C. Pfeiffer, B. Riaz, J. F. Schneiderman, H. Dong, S. min Hwang, L. You, B. Inglis, J. Clarke, M. A. Espy, R. J. Ilmoniemi, P. E. Magnelind, A. N. Matlashov, J. O. Nieminen, P. L. Volegov, K. C. J. Zevenhoven, N. Höfner, M. Burghoff, K. Enpuku, S. Y. Yang, J.-J. Chieh, J. Knuutila, P. Laine, and J. Nenonen, "SQUIDs in biomagnetism: a roadmap towards improved healthcare," *Superconductor Science and Technology*, vol. 29, no. 11, p. 113001, 2016. [Online]. Available: http://stacks.iop.org/0953-2048/29/i=11/a=113001

[10] Z. D. Grujić, P. A. Koss, G. Bison, and A. Weis, "A sensitive and accurate atomic magnetometer based on free spin precession," *The European Physical Journal D*, vol. 69, no. 5, p. 135, May 2015. [Online]. Available: https://doi.org/10.1140/epjd/e2015-50875-3

[11] H.-C. Koch, G. Bison, Z. D. Grujiċ, W. Heil, M. Kasprzak, P. Knowles, A. Kraft, A. Pazgalev, A. Schnabel, J. Voigt, and A. Weis, "Design and performance of an absolute ^{3}He/Cs magnetometer," *The European Physical Journal D*, vol. 69, no. 8, p. 202, Aug. 2015. [Online]. Available: https://doi.org/10.1140/epjd/e2015-60018-7

[12] D. Sheng, S. Li, N. Dural, and M. V. Romalis, "Subfemtotesla scalar atomic magnetometry using multipass cells," *Phys. Rev. Lett.*, vol. 110, p. 160802, Apr 2013. [Online]. Available: http://link.aps.org/doi/10.1103/PhysRevLett.110.160802

[13] M. E. Limes, E. L. Foley, T. W. Kornack, S. Caliga, S. McBride, A. Braun, W. Lee, V. G. Lucivero, and M. V. Romalis, "Total-field atomic gradiometer for unshielded portable magnetoencephalography," 2020.

[14] T. Scholtes, V. Schultze, R. IJsselsteijn, S. Woetzel, and H. G. Meyer, "Light-narrowed optically pumped M_x magnetometer with a miniaturized Cs cell," *Phys. Rev. A*, vol. 84, no. 4, OCT 12 2011.

[15] D. Hunter, S. Piccolomo, J. D. Pritchard, N. L. Brockie, T. E. Dyer, and E. Riis, "Free-induction-decay magnetometer based on a microfabricated Cs vapor cell," *Phys. Rev. Applied*, vol. 10, p. 014002, Jul 2018. [Online]. Available: https://link.aps.org/doi/10.1103/PhysRevApplied.10.014002

[16] G. Liu, J. Tang, Y. Yin, Y. Wang, B. Zhou, and B. Han, "Single-beam atomic magnetometer based on the transverse magnetic-modulation or dc-offset," *IEEE Sensors Journal*, vol. 20, no. 11, pp. 5827–5833, 2020.

[17] R. Zhang, T. Dyer, N. Brockie, R. Parsa, and R. Mhaskar, "Subpicotesla scalar atomic magnetometer with a microfabricated cell," *Journal of Applied Physics*, vol. 126, no. 12, p. 124503, 2019. [Online]. Available: https://doi.org/10.1063/1.5113520

[18] V. Shah, S. Knappe, P. D. D. Schwindt, and J. Kitching, "Subpicotesla atomic magnetometry with a microfabricated vapour cell," *Nat. Photon.*, vol. 1, no. 11, pp. 649–652, Nov. 2007. [Online]. Available: http://dx.doi.org/10.1038/nphoton.2007.201

[19] M. V. Romalis, E. Miron, and G. D. Cates, "Pressure broadening of rb D_1 and D_2 lines by ^{3}he, ^{4}he, n_2, and xe: Line cores and near wings," *Phys. Rev. A*, vol. 56, pp. 4569–4578, Dec 1997. [Online]. Available: http://link.aps.org/doi/10.1103/PhysRevA.56.4569

[20] C. Johnson, P. D. D. Schwindt, and M. Weisend, "Magnetoencephalography with a two-color pump-probe, fiber-coupled atomic magnetometer," *Applied Physics Letters*, vol. 97, no. 24, pp. –, 2010. [Online]. Available: http://scitation.aip.org/content/aip/journal/apl/97/24/10.1063/1.3522648

[21] G. Bevilacqua, V. Biancalana, P. Chessa, and Y. Dancheva, "Multichannel optical atomic magnetometer operating in unshielded environment," *Applied Physics B*, vol. 122, no. 4, pp. 1–9, 2016. [Online]. Available: http://dx.doi.org/10.1007/s00340-016-6375-2

[22] "Koheron 250 msps acquisition board," https://www.koheron.com/fpga/alpha250-signal-acquisition-generation.

[23] "Koheron software development kit," https://www.koheron.com/software-development-kit/.

[24] "Improving ADC Resoltion by Oversampling and Averaging," https://www.silabs.com/documents/public/application-notes/an118.pdf.

[25] H. G. Dehmelt, "Modulation of a light beam by precessing absorbing atoms," *Phys. Rev.*, vol. 105, pp. 1924–1925, Mar 1957. [Online]. Available: https://link.aps.org/doi/10.1103/PhysRev.105.1924

[26] W. E. Bell and A. L. Bloom, "Optically driven spin precession," *Physical Review Letters*, vol. 6, no. 6, pp. 280–&, 1961.

[27] V. Schultze, R. IJsselsteijn, T. Scholtes, S. Woetzel, and H.-G. Meyer, "Characteristics and performance of an intensity-modulated optically pumped magnetometer in comparison to the classical M_x magnetometer," *Opt. Express*, vol. 20, no. 13, pp. 14 201–14 212, 2012. [Online]. Available: http://www.opticsinfobase.org/abstract.cfm?uri=oe-20-13-14201

[28] Z. D. Grujìc and A. Weis, "Atomic magnetic resonance induced by amplitude-, frequency-, or polarization-modulated light," *Phys. Rev. A*, vol. 88, p. 012508, Jul 2013. [Online]. Available: http://link.aps.org/doi/10.1103/PhysRevA.88.012508

[29] H. Hai-Chao, D. Hai-Feng, H. Hui-Jie, and H. Xu-Yang, "Close-loop Bell–Bloom magnetometer with amplitude modulation," *Chinese Physics Letters*, vol. 32, no. 9, p. 098503, 2015. [Online]. Available: http://stacks.iop.org/0256-307X/32/i=9/a=098503

[30] C. Xu, S. G. Wang, Y. Y. Feng, L. Zhao, and L. J. Wang, "A self-sustaining atomic magnetometer with $1/\tau$ averaging property," *Scientific Reports*, vol. 6, p. 28169, Jun. 2016. [Online]. Available: http://dx.doi.org/10.1038/srep28169

[31] V. Gerginov, S. Krzyzewski, and S. Knappe, "Pulsed operation of a miniature scalar optically pumped magnetometer," *J. Opt. Soc. Am. B*, vol. 34, no. 7, pp. 1429–1434, Jul 2017. [Online]. Available: http://josab.osa.org/abstract.cfm?URI=josab-34-7-1429

[32] S. G. Kukolich, "Time dependence of quantum-state amplitudes demonstrated by free precession of spins," *American Journal of Physics*, vol. 36, no. 5, pp. 420–425, 1968. [Online]. Available: https://doi.org/10.1119/1.1974553

[33] S. Afach, G. Ban, G. Bison, K. Bodek, Z. Chowdhuri, Z. D. Grujić, L. Hayen, V. Hélaine, M. Kasprzak, K. Kirch, P. Knowles, H.-C. Koch, S. Komposch, A. Kozela, J. Krempel, B. Lauss, T. Lefort, Y. Lemière, A. Mtchedlishvili, O. Naviliat-Cuncic, F. M. Piegsa, P. N. Prashanth, G. Quéméner, M. Rawlik, D. Ries, S. Roccia, D. Rozpedzik, P. Schmidt-Wellenburg, N. Severjins, A. Weis, E. Wursten, G. Wyszynski, J. Zejma, and G. Zsigmond, "Highly stable atomic vector magnetometer based on free spin precession," *Opt. Express*, vol. 23, no. 17, pp. 22 108–22 115, Aug 2015. [Online]. Available: http://www.opticsexpress.org/abstract.cfm?URI=oe-23-17-22108

[34] N. Wilson, C. Perrella, R. Anderson, A. Luiten, and P. Light, "Wide-bandwidth atomic magnetometry via instantaneous-phase retrieval," *Phys. Rev. Research*, vol. 2, p. 013213, Feb 2020. [Online]. Available: https://link.aps.org/doi/10.1103/PhysRevResearch.2.013213

[35] S. Li, P. Vachaspati, D. Sheng, N. Dural, and M. V. Romalis, "Optical rotation in excess of 100 rad generated by Rb vapor in a multipass cell," *Phys. Rev. A*, vol. 84, p. 061403, Dec 2011. [Online]. Available: https://link.aps.org/doi/10.1103/PhysRevA.84.061403

[36] A. Borna, T. R. Carter, P. DeRego, C. D. James, and P. D. D. Schwindt, "Magnetic source imaging using a pulsed optically pumped magnetometer array," *IEEE Transactions on Instrumentation and Measurement*, pp. 1–9, 2018.

[37] V. G. Lucivero, W. Lee, M. E. Limes, E. L. Foley, T. W. Kornack, and M. V. Romalis, "A femtotesla quantum-noise-limited pulsed gradiometer at finite fields," in *Quantum Information and Measurement (QIM) V: Quantum Technologies*. Optical Society of America, 2019, p. T3C.3. [Online]. Available: http://www.osapublishing.org/abstract.cfm?URI=QIM-2019-T3C.3

[38] S. J. Smullin, I. M. Savukov, G. Vasilakis, R. K. Ghosh, and M. V. Romalis, "Low-noise high-density alkali-metal scalar magnetometer," *Phys. Rev. A*, vol. 80, p. 033420, Sep 2009. [Online]. Available: https://link.aps.org/doi/10.1103/PhysRevA.80.033420

[39] L.-A. Liew, S. Knappe, J. Moreland, H. Robinson, L. Hollberg, and J. Kitching, "Microfabricated alkali atom vapor cells," *Applied Physics Letters*, vol. 84, no. 14, pp. 2694–2696, 2004. [Online]. Available: https://doi.org/10.1063/1.1691490

[40] R. Zhang, R. Mhaskar, K. Smith, and M. Prouty, "Portable intrinsic gradiometer for ultra-sensitive detection of magnetic gradient in unshielded environment," *Applied Physics Letters*, vol. 116, no. 14, p. 143501, 2020. [Online]. Available: https://doi.org/10.1063/5.0004746

[41] J. Kitching, "Chip-scale atomic devices," *Applied Physics Reviews*, vol. 5, no. 3, p. 031302, 2018. [Online]. Available: https://doi.org/10.1063/1.5026238

[42] E. Boto, N. Holmes, J. Leggett, G. Roberts, V. Shah, S. S. Meyer, L. D. Muñoz, K. J. Mullinger, T. M. Tierney, S. Bestmann, G. R. Barnes, R. Bowtell, and M. J. Brookes, "Moving magnetoencephalography towards real-world applications with a wearable system," *Nature*, Mar. 2018. [Online]. Available: http://dx.doi.org/10.1038/nature26147

Vladislav Gerginov received his M.Sc. degree from the Sofia University "St. Kl Ohridski", Sofia, Bulgaria in 1995, and his PhD degree from the University of Notre Dame, Notre Dame, IN in 2003. Between 2002 and 2006 he was a Postdoctoral Associate at the National Institute of Standards and Technology (NIST) in the United States, working on precision frequency measurements and NIST's chip-scale atomic clock. Between 2008 and 2016 he was a staff scientist at the Physikalisch-Technische Bundesanstalt (PTB) in Germany, working on primary frequency standards. He joined the University of Colorado, Boulder as a Senior Research Associate in 2016, and is currently involved in the development of atomic frequency references and highly-sensitive quantum sensors. His primary areas of research are precision spectroscopy, atomic clocks and atomic magnetometry.

Marco Pomponio received his M. Sc. degree in electronic engineering from the Polytechnic of Turin, Italy in 2017. During his thesis work he focused on a digital Field Programmable Gate Array (FPGA) approach to control and manage quantum physics experiments. In 2018 he presented his work at the European Frequency and Time Forum (EFTF), which won a student competition. He started working at the National Institute of Standards and Technology in 2018. His main tasks are the research and development of high-performance digital control loops, signal processing and custom electronics for various applications in the Time and Frequency Division of NIST.

Svenja Knappe received her Ph.D. in physics from the University of Bonn, Germany in 2001 with a thesis on miniature optically-pumped magnetometers and atomic clocks based on coherent-population trapping. For 16 years, she worked at the National Institute of Standards and Technology (NIST) in Boulder CO, developing chip-scale atomic sensors. She is now an Associate Research Professor at the University of Colorado and her research interests include microfabricated atomic sensors. She is also a co-founder of FieldLine Inc., a startup company located in Boulder CO, developing magnetic sensing and imaging solutions based on quantum sensors.